



A dealloyed bulk FeNi pattern with exposed highly active facets for cost-effective oxygen evolution

Weiliang Peng ^{a,b}, Yuyin Li ^c, Bin Yuan ^{a,b,*}, Renzong Hu ^{a,b}, Zhengtang Luo ^{c, **}, Min Zhu ^{a,b,*}

^a School of Materials Science and Engineering, South China University of Technology, Guangzhou 510640, PR China

^b Key Laboratory of Advanced Energy Storage Materials of Guangdong Province, PR China

^c Department of Chemical and Biological Engineering, Hong Kong University of Science and Technology, Clear Water Bay, Kowloon 999077, Hong Kong, China



ARTICLE INFO

Keywords:

FeNi alloy
Preferential etching
Self-supporting electrodes
Oxygen evolution reaction
Water splitting

ABSTRACT

Porous materials are attractive substrates for oxygen evolution reaction (OER), however, suffer from sluggish kinetics because of weak catalyst-support interaction and low conductivity. Here, a porous FeNi alloy layer with exposed high active facets was developed on commercially-available bulk FeNi materials. The designed hierarchical structure can significantly promote the interaction between substrate and Ni-Fe layered double hydroxide catalyst, and remain high conductivity of bulk metal substrate. The obtained OER electrode exhibits an ultra-small overpotential of 298 mV to deliver industrial required current density of 1000 mA cm^{-2} , while retaining catalytic activity for 1350 h at room temperature and over 100 h even at 80 °C. Notably, the alkaline water electrolyzer using this OER electrode exhibits a super-low voltage of 1.46 V for a current density of 10 mA cm^{-2} . Our novel strategy opens up an inexpensive solution for the design of OER electrodes with high catalytic activity and excellent stability.

1. Introduction

Electrochemical water splitting converts electricity into low-price and clean hydrogen energy, which eventually may solve the challenge of renewable energy utilization and achieve carbon reduction all over the world [1–3]. The oxygen evolution reaction (OER) is considered as a vital half-reaction and bottleneck of overall water splitting due to its sluggish kinetics [4]. Thus, OER electrodes with high catalytic activity and long-term stability are imminently demanded. Compared with the noble metal Ru/Ir-based catalysts, the transition metal(TM)-based OER electrocatalysts, including layered double hydroxides (LDH) [5–7], nitrides [8,9], borides [10,11], sulfides [12,13] and phosphides [14,15], are promising candidates for large-scale industrial applications because of their low-cost and high earth-abundant [16].

To enhance the catalytic performances of TM-based OER electrode, the general strategies include increasing the catalytic active sites per unit geometric areas, and enhancing the intrinsic activity of TM-based catalysts [17]. In fact, porous materials with high specific surface area, especially commercial nickel foam (NF) are widely used as substrates to load TM-based electrocatalysts modified by designing morphology [12, 18], optimizing elements composition [9,19], creating defects [20,21],

etc., resulting in the relatively excellent catalytic activity of these prepared OER electrodes (sometimes even superior to noble metal electrodes). Although great progresses on OER catalytic activity of these TM-based electrodes have been made upon lab conditions (e.g. OER current density of 10 mA cm^{-2} and room temperature), it exists still a huge gap to employing these OER electrodes under industrially relevant conditions (e.g. OER current density of 1000 mA cm^{-2} to be generated at low overpotential of $< 300 \text{ mV}$, 60–80 °C and long-term operational stability are urgently required for low-price alkaline water electrolyzer [4,18,22]). The main problem of long-time catalytic stability of OER electrodes at high current density originates from structural degeneration of high-performance catalysts (e.g. loss or transformation of high active sites or beneficial interface) [4,18,23–27] and weak interaction with conductive substrate during OER (e.g. low bonding strength or high interface resistance) [6,18,23,25,28,29]. Thus, developing low-price OER electrodes with highly catalytic activity and long-term stability (e.g. as least one thousand hours) under industrially harsh conditions still remain a huge challenge. Specially, commercial porous materials suffer from poor inter-pore connection, unitary micro-scale pore structure and low surface energy that lead to weak catalyst-support interaction and complicated interfaces [7,23], which do not satisfy the

* Corresponding authors at: School of Materials Science and Engineering, South China University of Technology, Guangzhou 510640, PR China.

** Corresponding author.

E-mail addresses: apsheng@scut.edu.cn (B. Yuan), keztluo@ust.hk (Z. Luo), memzhu@scut.edu.cn (M. Zhu).

requirements of porous substrate for OER electrodes under industrially harsh conditions, but the research on tackling this issue is extremely lacking.

Recently work[7] shows that Ni-Fe layered double hydroxide (NiFe-LDH, considered as the most promising earth-abundant OER catalyst[30]) *in situ* grown on bulk FeNi alloy foil with (111)-oriented exposed facet (FCC austenite structure) exhibits an ultra-small onset overpotential because of the unique interfacial layer that enhances adsorption of the OH intermediate compared with bulk Ni or Fe foil. However, the details of intrinsic catalytic activity and long-term stability under real-operation conditions are not entirely clear. In addition, it is also hard and costly to obtain the Fe-Ni alloy foil substrate with high specific surface area (such as porous structure still with (111)-oriented exposed facet) to support NiFe-LDH for further improving the catalytic activity. Besides, it has been well accepted that catalytic performance of exposed facets are correlated with surface energies (γ) in the order of $\gamma(111) < \gamma(100) < \gamma(110)$ for FCC nano-sized crystals[31]. Furthermore, it has been confirmed that the engineering of high-energy interfacial structures is an effective approach to design highly active and ultra-stable OER nano-sized catalysts[13,32]. However, it is still a big challenge to construct a high-energy interface between porous substrate and nano-sized catalysts with high active exposed facets. Considering the above several aspects, it is obvious that more efforts should be undertaken to design and construct a porous substrate with exposed highly active facets that can meet the requirements for OER electrodes under industrially harsh conditions, where keep economically viable cost.

Herein, we developed a cost-effective and energy-efficient dealloying method to fabricate a gradient porous FeNi layer with high active facets on low-cost commercially-available bulk FeNi alloy (Permalloy trademark 1J36). The dealloyed hierarchical structure can result in a reasonable three-phase interface and strong interaction effect between FeNi substrate and NiFe-LDH catalyst. The obtained OER electrode exhibits superior intrinsic catalytic activity and long-term stability under alkaline environments. To the best of our knowledge, it achieves the record of highest intrinsic catalytic activity of 243 mV to reach a current density of 10 mA cm^{-2} (electrochemical active surface area). Notably, it can reach the criterions of large-scale industrial application for delivering current density of 1000 mA cm^{-2} at an ultra-low overpotential of 298 mV for more than 1350 h at room temperature and over 100 h even at 30 wt% KOH and 80 °C.

2. Experimental section

2.1. Preparation of porous FeNi alloy substrate

Porous FeNi alloy substrates were prepared via a dealloying method at room temperature. Firstly, a batch of FeNi alloy sheets ($5 \times 1.5 \text{ cm}^2$, thickness: 0.8 mm) were polished using 1000# polishing paper and washed by ethanol and water alternately under ultrasonication for 10 min. Secondly, these pretreated FeNi alloy sheets were transferred into a 100 ml aqueous solution containing 50 mmol $\text{FeCl}_3 \cdot 6\text{H}_2\text{O}$ and 25 mmol $\text{Na}_2\text{S}_2\text{O}_8$ for 1–5 h with a very slow magnetic stirring. Subsequently, the sheets were rinsed with distilled water, ethanol each for several times, and dried at 50 °C for 2 h in a drying oven.

2.2. *In situ* growth of NiFe-LDH on DFN-4, BFN and NF

The NiFe-LDH was synthesized according to the previous work[7] but with a little modification. Typically, a solution of $\text{Fe}(\text{NO}_3)_3 \cdot 9\text{H}_2\text{O}$ (1 mmol), $\text{Ni}(\text{NO}_3)_2 \cdot 6\text{H}_2\text{O}$ (1 mmol) and urea (10 mmol) was dissolved in 72 ml DI water with stirring. Then, the solution and the substrates (DFN-4, BFN and NF) were transferred to the 100 ml Teflon-lined stainless-steel autoclaves, which were heated at 120 °C for 12 h and cooled to room temperature naturally. Subsequently, the self-supported electrodes were rinsed with distilled water, ethanol each for several times, and dried at 50 °C for 2 h in a drying oven.

2.3. Characterizations

The structure of the as-prepared samples was characterized by an X-ray diffractometer (XRD, Empyrean, Malvern Panalytical) with $\text{Cu K}\alpha$ radiation ($\lambda = 0.1541 \text{ nm}$). The elemental composition and surface morphology were analyzed using energy dispersive analysis (EDS, XFlash Detector 5010, Bruker) and scanning electron microscopy (SEM, Super 40, Zeiss). The X-ray photoelectron spectroscopy (XPS) was performed with a PerkinElmer PHI 5000c XPS system using the C 1 s peak at 285.0 eV as a reference. The transmission electron microscope (TEM) images were obtained with an FEI Talos F200X operating at 200 kV. The electronic conductivity of the samples was measured by a four-probe method (RTS-9, Four Probes Tech). The contact angle of the samples was evaluated using optical contact angle measuring and contour analysis systems (OCA40 Micro, DATA physics). The three-dimensional surface topography of the samples was performed with a 3D optical profiler (RTEC UP series, Rtec-Instruments).

2.4. Electrochemical measurements

Electrochemical OER measurements were performed with a Gamry Interface 1000 electrochemical workstation in a standard three-electrode system at room temperature or 80 °C. The as-prepared samples were used as the working electrodes with a geometric area of 0.25 cm^2 . The Pt plate was used as counter electrode. The Hg/HgO and Ag/AgCl electrodes were used as the reference electrodes at room temperature and 80 °C, respectively. The normal electrochemical measurements were carried out in 1.0 M KOH solution at room temperature and all potentials were calibrated to the reversible hydrogen electrode (RHE) by using the equation: $E_{\text{RHE}} = E_{\text{Hg}/\text{HgO}} + 0.098 + 0.059 \times pH$ ($pH = 14$). When the stability test performs in 30 wt% KOH ($pH = 14.7$) at 80 °C, the potential of Ag/AgCl reference electrode was calibrated via a homemade RHE system, that is, the zero current potential determined by cyclic voltammetry (0.5 mV s^{-1}) at the potential windows of hydrogen evolution reaction using two Pt electrodes as working electrode and counter electrode. Linear sweep voltammetry (LSV) curves were recorded at a scan rate of 5 mV s^{-1} . Before recording, the as-prepared samples firstly was scanned for 20 cyclic voltammetry (CV) cycles between -0.35 and 0.65 V (vs. Hg/HgO) at 100 mV s^{-1} until a stable cyclic voltammogram was recorded. Polarization curves were corrected by the current interrupt method in the Gamry electrochemical workstation. The Tafel plots were fitted into the Tafel equation ($\eta = b \log j + a$, where η is the overpotential and j is the current density). The long-term stability performance was measured by chronopotentiometric measurement at various current densities. The electrolyte is replaced with fresh KOH solution per 50 h in long-term stability test. The electrochemical impedance spectroscopy (EIS) tests were performed under a given overpotential in a frequency range from 100 kHz to 0.1 Hz with a 5 mV amplitude.

2.5. DFT calculation details

DFT calculations were performed using Vienna Ab Initio Simulation Package (VASP) with generalized gradient approximation (GGA) based on the Perdew–Burke–Ernzerhof (PBE) exchange–correlation functional [33,34]. For all calculations, the kinetic cut-off energy for plane wave truncation was set to 450 eV with the energy change convergence criterion of $1 \times 10^{-5} \text{ eV}$. And the equilibrium geometries were obtained when atomic forces were less than $0.02 \text{ eV}/\text{\AA}$. More details about surface energy, adsorption energy and Gibbs free energy diagram can be found in the [Supporting Information](#).

3. Results and discussion

3.1. DFT simulations of FeNi substrate

Fig. 1a illustrates the DFT calculations of surface energies, which were performed based on the bulk structures of Ni and FeNi (inset of Fig. 1a). As shown in Fig. 1a and Table S1 (Supporting Information), the surface energies of the FeNi alloy are higher than that of pure Ni for the same Miller indices. It should be noted that the (220) facet of FeNi alloy exhibits the highest surface energy of 3.17 J/m^2 , indicating relative higher hydrophilicity and aerophobicity on (220) facet of FeNi alloy [35], favoring mass diffusion and the release of gas bubbles during gas evolution reaction, and then resulting in boosted OER kinetics. As shown in Fig. 1b and Table S2-S4, the calculated adsorption energies on different substrates among various possible adsorption sites (Fig. S1-S3) reveals OH^- is prone to adsorb on the surface of FeNi(220) substrate with an adsorption energy of -3.68 eV , lower than that of FeNi(111) substrate (-3.13 eV) and Ni(111) substrate (-2.75 eV). Based on the classical adsorbate evolution mechanism (AEM) of OER under alkaline environments (see the Supporting Information for details)[5,24], it should be noted that OH^- participates in every step during the OER process. Therefore, FeNi(220) substrate with lower adsorption energy of OH^- possess more favorable enhancement to OER process[20,21]. As a result, FeNi(220) substrate would lead to higher OER performance from above two aspects when served as electrode directly, compared with FeNi(111) and Ni(111) substrates. More importantly, the superior wettability and lower adsorption energy (OH^-) of FeNi(220) substrate make hydroxides more likely to nucleate and grow on the surface and

stabilize the active sites, resulting in the better robustness and faster electron transfer between catalyst and substrate, implying stronger catalyst-support interactions. Thus, FeNi(220) substrate would be more suitable as the conductive substrate to support the hydroxide catalyst, compared with FeNi(111) and Ni(111) substrates.

3.2. Preparation and characterization of porous FeNi substrate

Obviously, DFT calculated results show that the FeNi alloy with exposed (220) facets is a promising substrate for self-supporting OER electrode due to the potential strong catalyst-support interaction. According to the reported work of selective etching[36], those facets with higher surface energies can be etched faster and tend to be exposed on the surface after etching. For this reason, the porous FeNi(220) substrate was prepared by a simple dealloying method, (denoted as DFN-n, n is the dealloying duration in hour). As schematically shown in Fig. 1c, the bare FeNi (BFN) alloy sheets were transferred into an aqueous solution containing $\text{FeCl}_3 \cdot 6\text{H}_2\text{O}$ and $\text{Na}_2\text{S}_2\text{O}_8$ for 4 h to form the porous FeNi(220) substrate (DFN-4). Fig. 1d presents the cross-sectional SEM image of the DFN-4, and it clearly reveals the hierarchical structure of a porous surface layer with a dense core. Furthermore, Fig. 1e displays the three-dimensional surface topography of the DFN-4 by a 3D optical profiler, it indicates that the thickness of the porous layer is about $80 \mu\text{m}$, which can boost the accessible active sites dramatically in comparison with the BFN substrate.

The evolution of the surface morphology of FeNi alloy during dealloying, is shown in Figs. 2a-2b, Fig. S4 and Fig. S5. The surfaces of BFN are relatively smooth before dealloying (Fig. S4), and become rough

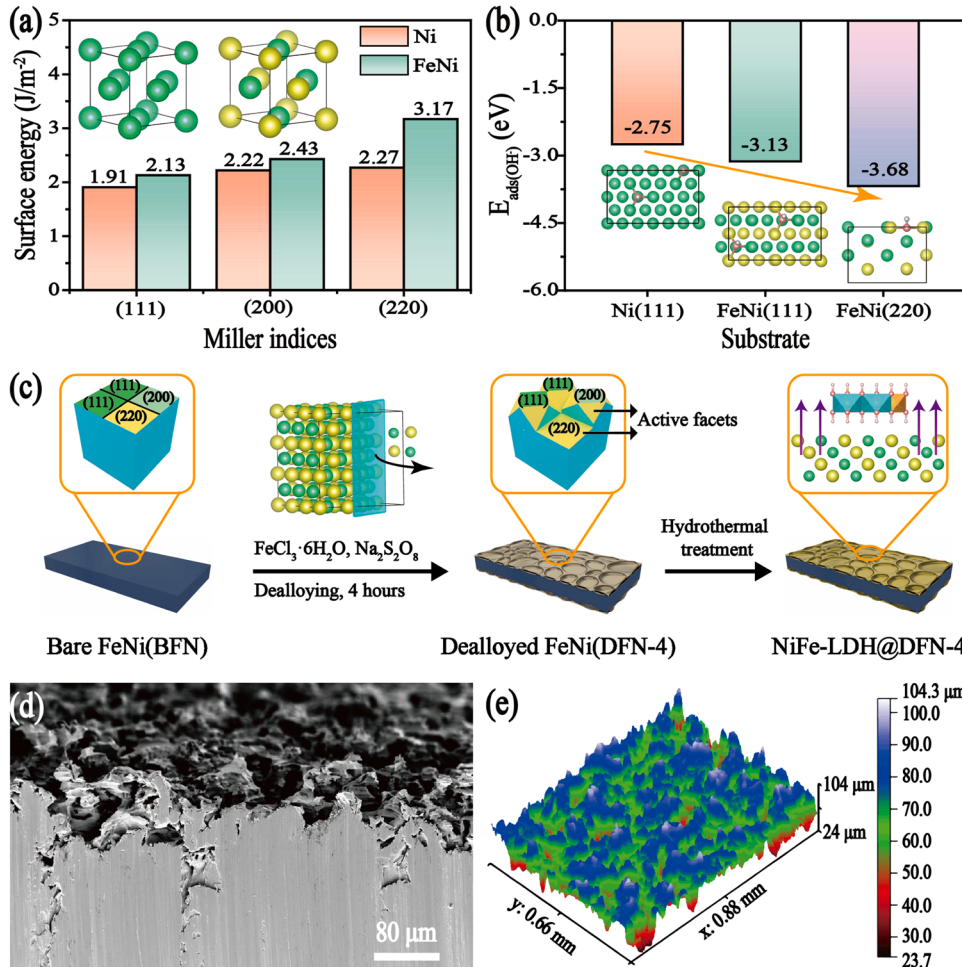


Fig. 1. DFT calculation and the corresponding design strategy of self-supporting OER electrode. Here green is Ni atom, yellow is Fe atom, red is O atom and gray is H atom. (a) Surface energies of Ni and FeNi (inset: bulk structures of Ni and FeNi). (b) Adsorption energies for OH^- on different substrates (inset: adsorption models). (c) Schematic illustration of the preparation process of the porous FeNi alloy substrate and self-supported OER electrode. (d) Cross-sectional SEM image of DFN-4. (e) Three-dimensional surface topography of DFN-4. Results show that FeNi(220) substrate can be considered as the promising substrate for self-supporting OER electrode compared with FeNi(111) and Ni(111) substrates.

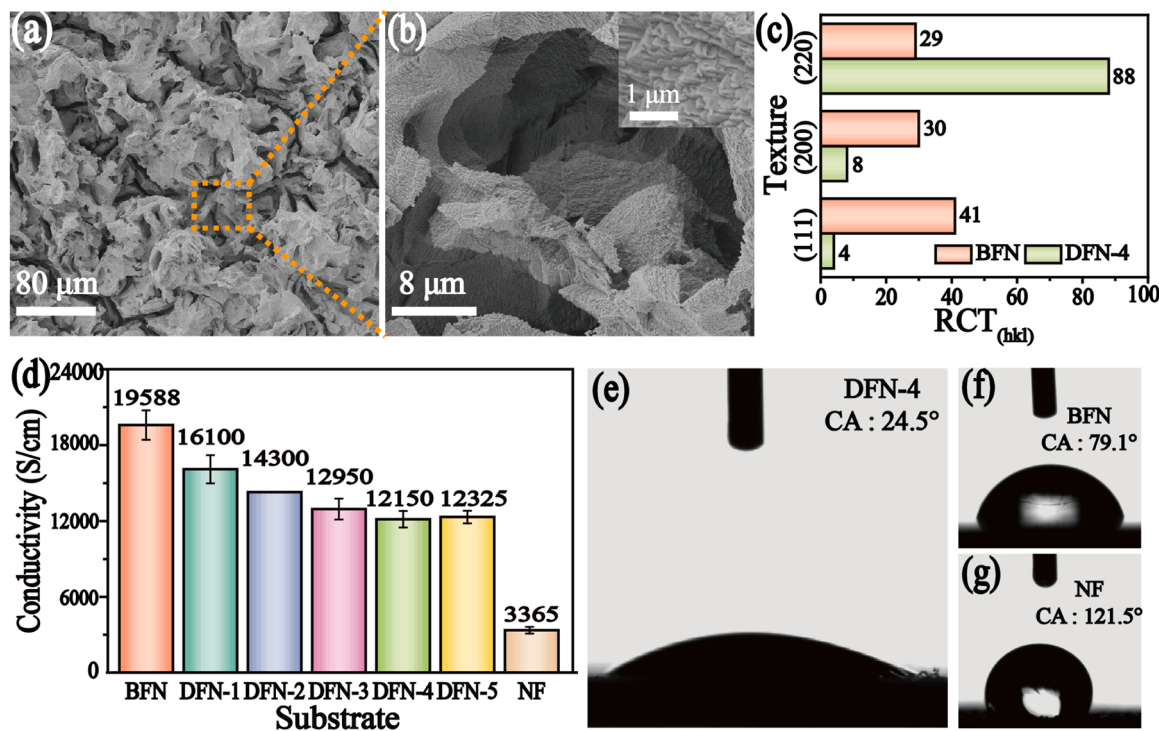


Fig. 2. Porous FeNi alloy substrates. (a) and (b) surface morphologies of DFN-4; (c) Histograms for fitted relative texture coefficient (RTC) of BFN and DFN-4; (d) The electronic conductivity of the BFN, DFN-n ($n = 1-5$) and commercial nickel foam (NF); The water contact angles (CA) of DFN-4 (e), BFN (f) and NF (g). After dealloying treatment of 4 h, the unique porous FeNi alloy substrate (DFN-4) with reasonable design has been fabricated.

with isolated pores (sample DFN-1, Fig. S5a) and the trend continues for 2 h and 3 h etching. When the dealloying is further increased to 4 h, the surface of DFN-4 appears a lot of interconnected pores and cracks (Fig. 2a), with the diameter of pores is $\sim 20 \mu\text{m}$ (Fig. 2b), with nano-size polyhedral mastoids on pore walls (inset of Fig. 2b). Further etching to DFN-5 (Fig. S5d) does not change the morphology further. The electrochemical active surface area (ECSA) was derived from the double layer capacitance (C_{dl}) (Fig. S6 and Fig. S7), and obtained values 6.73, 7.70, 7.83, 8.85 and 8.78 cm^2 , for DFN-n ($n = 1-5$) respectively. The ECSA of the DFN-4 is 1.8 times larger than that of the BFN, suggesting the DFN-4 possesses a higher density of active sites per unit geometric area for oxygen evolution reaction [37]. These results are consistent with the abovementioned SEM observation. Additionally, we obtained the Fe and Ni contents of BFN and DFN-4, shown in Table S5. Interestingly, the Fe content of DFN-4 increases compared with that of BFN, while the Ni content of DFN-4 decreases, not following the electrochemical potential difference between Fe and Ni. This abnormal phenomenon may be due to the inhibitory effect of reaction product Fe^{2+} on Eq. 1, resulting in the faster releasing of Ni via an oxidation etching of Fe^{3+} (Eq. 2), owing to the electrochemical potential difference between $E^\theta(\text{Fe}^{2+}/\text{Fe}^{3+})$ (0.771 V) and $E^\theta(\text{Ni}^0/\text{Ni}^{2+})$ (-0.257 V) [19]. Besides, the newly formed Fe^{2+} will be gradually oxidized to Fe^{3+} by $\text{S}_2\text{O}_8^{2-}$ (Eq. 3) [38], which can promote the dealloying (Fig. S8).



During the process of dealloying, it is found that (220) facets of FeNi alloy with higher surface energies can be selectively etched at a higher rate, resulting in the exposure of (220) facets and the formation of pores in our case [36]. Fig. S9 shows X-ray diffraction (XRD) patterns of the samples. The peaks of BFN at 43.9° , 50.9° and 74.8° are assigned to $\text{Fe}_{0.64}\text{Ni}_{0.36}$, a single phase FCC austenite structure (JCPDS no.

047-1405). The patterns of DFN-n ($n = 1-5$) with the similar peak position imply that the samples exhibit the same phase with same crystal structure. X-ray photoelectron spectroscopy (XPS) spectra show that there is a higher concentration of hydroxide species and defect sites in the DFN-4 (Fig. S10-S12, see the Supporting Information for details), but below the detection limit of XRD, implying better OER performance of DFN-4, compared with the BFN. In order to further quantify the preferred orientation of DFN-4 formed by etching, the relative texture coefficient (RTC) was calculated (see the Supporting Information for details) [39]. The results reveal that the RTC of (220) facets increased from 29 of the BFN to 88 of the DFN-4, as shown in Fig. 2c, indicating the main preferred orientation in the porous layer of DFN-4 is (220) facets, which are more likely to be exposed to the basal surface, which conforms with our strategy [39]. Meanwhile, the selective etching of (220) facets results in the formation of micro-pores in the sectional direction due to the non-parallel relationship between the (220) facets and the basal surface.

The electronic conductivities of these substrates are given in Fig. 2d. Surprisingly, the electrical conductivity of DFN-4 (12510 S cm^{-1} , 62% of BFN) is about 4 times higher than that of commercial NF (3365 S cm^{-1}), because the core dense layer of the DFN-4 can provide an electron transport highway [18,20], indicating that contact resistance is highly reduced, and therefore improving electrolysis efficiency. In addition, the surface wettability of the DFN-4, BFN and commercial NF are given in Figs. 2e-2g. The water contact angle of the DFN-4 reaches as low as 24.5° , while the water contact angle for the BFN and commercial NF are 79.1° and 121.5° , respectively, indicating the superior wettability for the DFN-4, as well as superior aerophobicity according to wetting theory that a superhydrophilic surface is superaerophobic in the electrolyte [27, 35]. In short, those remarkable properties are attributed to the high surface energy of (220) facets and discontinuous three-phase contact line of O_2 (gas), electrolyte (liquid) and electrode (solid) caused by micro-nano scale hierarchical structure [26]. Thus, electrolytes can infiltrate into interior pore of the DFN-4 easily and increase greatly the contact surface with the electrodes, and then produced gas bubbles can

be released quickly, which accelerates electrolytes access to the catalytic active sites and enhances the mass transfer during the process of OER [12,18,26]. Above results demonstrate the reasonable designed porous FeNi substrate has been fabricated.

The OER performances of different substrates were evaluated in a typical three-electrode system in 1.0 M KOH (Fig. S13-S20, see the Supporting Information for details). The OER activities of the as-prepared series of DFN-n render much lower onset potential and higher current densities compared with the commercial NF and BFN, which is consistent with our designed strategy. It is well known that FeNi substrate exhibit good OER catalytic activity due to nanosized FeNi hydroxides randomly formed on the surface[40]. Moreover, it can be seen that the DFN-4 exhibits the best OER catalytic performance with low potentials of only 301, 345 and 370 mV to reach current densities of 10, 100 and 250 mA cm⁻², respectively, and is superior to the others DFN-n (n = 1, 2, 3, 5) substrates (Fig. S13). Notably, the DFN-4 shows

much better thermodynamic and kinetic than the available reported OER substrates (Fig. S17 and Table. S7) in 1 M KOH. Besides, the DFN-4 possesses long-term durability under the operating condition for 40 h without detectable current density decay (Fig. S18), suggesting its potential for industrial applications.

3.3. Preparation and characterization of the self-supporting electrodes

The porous FeNi alloy substrate can be further strengthened by loading various of well-designed and high performance OER nanocatalysts like others porous substrates to reduce the overpotential. It is evident that more efforts should be undertaken to further reveal the influence of strong catalyst-support interaction and reasonable three-phase interface induced by reasonable designed porous FeNi substrate with exposed high energy facets on intrinsic catalytic activity and long-term stability. As a proof-of-concept application, low-cost and high-

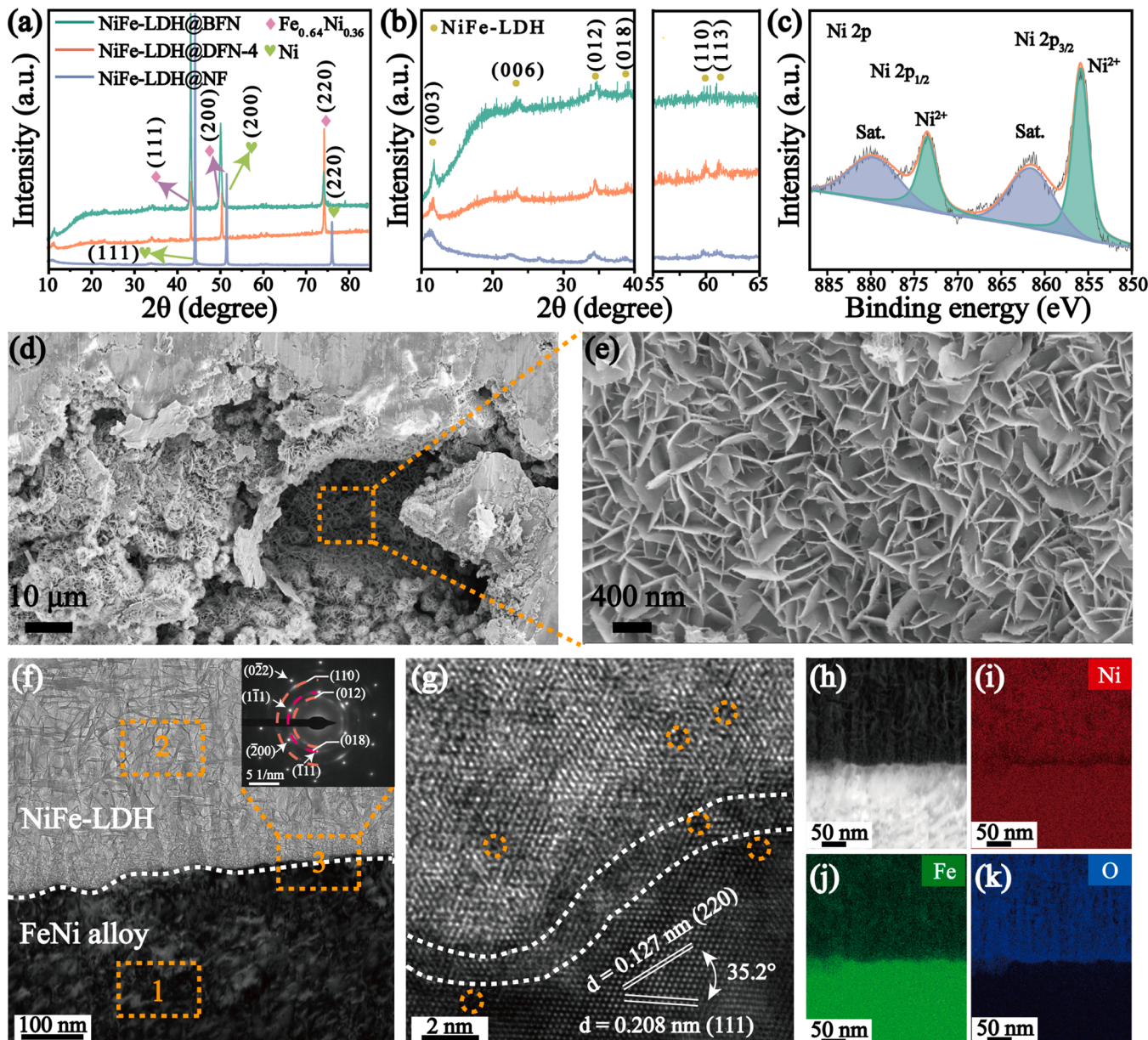


Fig. 3. As-prepared self-supported OER electrodes. (a) XRD patterns; (b) Partial enlargement curves in (a); (c) The high-resolution XPS spectra in the regions of Ni 2p for NiFe-LDH@DFN-4; (d & e) SEM images for a cross-section of NiFe-LDH@DFN-4; (f) TEM image for a cross-section of NiFe-LDH@DFN-4 with an inset showing the SAED pattern of region 3; (g) HRTEM image for a cross-section of NiFe-LDH@DFN-4; (h) HAADF image for a cross-section of NiFe-LDH@DFN-4 and corresponding EDX mapping images of Ni (i), Fe (j) and O (k) elements.

performance NiFe-LDH nano-arrays serving as a catalyst model[30] were *in situ* grown on the substrate of the DFN-4 (see Fig. 1c and the Experimental Section for details). The BFN (FeNi alloy with main orientation of (111)) and commercial NF (Ni with main orientation of (111)) were also employed as conductive substrate to support the NiFe-LDH catalyst as controls. As shown in Fig. 3a, XRD patterns of the as-prepared self-supported electrodes show strong diffraction peaks of FeNi austenite or metallic Ni, along with NiFe based hydroxide diffraction peaks at 11.47°, 34.43° and 60.28° (Fig. 3b), matching well with the typical pattern of NiFe-LDH (JCPDS no.040-0215)[41]. The elemental chemical states of NiFe-LDH@DFN-4 were further investigated by XPS. As clearly illustrated in Fig. 3c, the binding energy peaks of Ni 2p_{1/2} and Ni 2p_{3/2} located in 873.5 and 855.9 eV[7] are assigned to Ni²⁺. The two main binding energy peaks of Fe 2p at 724.9 eV and 712.0 eV[7,22] are the typical peaks of Fe³⁺ (Fig. S21). Correspondingly, the spectrum in the regions of O1s can be divided into three peaks located at 529.7 eV (O1), 531.2 eV (O2) and 532.8 eV (O3), which match typical metal-oxygen bands, hydroxide species and chemically absorbed water, respectively (Fig. S21)[22,38]. The elemental chemical states of NiFe-LDH@BFN and NiFe-LDH@NF show similar results (Fig. S22-S23). Besides, the surface morphologies of NiFe-LDH nano-sheet arrays on different substrates were observed by SEM. Apparently, the well-defined nanosheets grow vertically on the pores of porous FeNi alloy substrate (Fig. 3d), forming successfully a uniform porous NiFe-LDH layer with abundant active sites (Fig. 3e). The grown NiFe-LDH on the BFN and commercial NF show similar morphologies of nanosheets grown vertically (Fig. S24-S25).

To uncover the interface of the DFN-4 and NiFe-LDH in the vertical direction, the cross-sectional transmission electron microscope (TEM) was performed using focused ion beam (FIB) technique. As shown in Fig. 3f, it can be clearly seen that the NiFe-LDH@DFN-4 is composed of two phases of FeNi alloy and NiFe-LDH with corresponding selected area electron diffraction (SAED) patterns of region 1 and region 2 (Fig. S26). And its corresponding SAED pattern of region 3 (inset of Fig. 3f) confirms the two phases, consistent with the XRD results, and the high-resolution transmission electron microscope (HRTEM) image and the corresponding fast Fourier transform (FFT) patterns (Fig. S27-S28). Moreover, as shown in Fig. 3g and Fig. S27,

the interface boundary of two phases is flexuous due to the unique pore structure of DFN-4 by etching. It can be seen that the lattice fringe of FeNi alloy near the interface boundary show interplanar distances of 0.208 and 0.127 nm, corresponding to the (111) and (220) facets with an angle of 35.2°, and we clearly observe some interface areas where NiFe-LDH grow on the (220) facets of FeNi alloy, which conforms with our strategy of designing interface between FeNi (220) facets and NiFe-LDH to induce potential strong catalyst-support interaction. It should be noted that there are some defects in both FeNi alloy and NiFe-LDH near the interface as indicated by the dashed circles in Fig. 3g, which should be a result of the (220) facets with atomic unsaturated coordination and may enhance the OER catalytic activity of NiFe-LDH@DFN-4. Furthermore, we obtained the high-angle annular dark-field (HAADF) image and element mappings. As shown in Figs. 3h-3k, the strong signals from Ni and Fe elements at the bottom layer indicate the homogeneous distribution of Ni and Fe elements in the DFN-4 substrate. Comparatively, it shows that the slight signals of Ni and Fe elements, and the strong signal of O element at the top layer are uniformly distributed, which is consistent with NiFe-LDH.

3.4. Electrochemical evaluation of the self-supporting electrodes for OER

To further evaluate the OER performances, the as-prepared NiFe-LDH@DFN-4 electrode, was directly applied to a three-electrode system in 1 M KOH electrolyte. The NiFe-LDH@BFN and NiFe-LDH@NF electrodes were also tested as controls to highlight the strong catalyst-support interaction between DFN-4 substrate with exposed FeNi(220) facet and NiFe-LDH catalyst. As illustrated in Fig. 4a, the NiFe-LDH@NF

possesses an apparent oxidation peak at around 1.43 V (vs. RHE), which can be attributed to the oxidation of nickel-based catalyst (Ni²⁺ → Ni³⁺) [42-44]. The signal overlap between the transformation of Ni²⁺/Ni³⁺ and oxygen evolution exists in the polarization curves of the NiFe-LDH@DFN-4 and NiFe-LDH@BFN, resulting in the non-prominent oxidation peak. However, the redox phenomenon of Ni²⁺/Ni³⁺ can be demonstrated in the CV curves of the activation process (Fig. S29). Compared with the NiFe-LDH@BFN, the NiFe-LDH@NF exhibits stronger OER response due to more exposed catalytic active sites, indicating the advantages of using porous materials with high specific surface area as conductive substrate. Surprisingly, the NiFe-LDH@DFN-4 shows the remarkably enhanced OER catalytic activity with a low overpotential of 231 mV at a current density of 100 mA cm⁻², which is obviously superior to that of NiFe-LDH grown on commercial NF, and even the commercial noble metal-based catalyst (IrO₂) supported on commercial NF (IrO₂/NF), indicating the DFN-4 is more suitable as the porous conductive substrate to support NiFe-LDH catalyst compared with commercial NF. In particular, at higher current densities of 500 and 1000 mA cm⁻², the NiFe-LDH@DFN-4 exhibits ultra-low overpotential of 272 mV and 298 mV, matching the requirement of overpotential for industrial large-scale applications[18,22]. The overpotentials at various current densities of the NiFe-LDH@DFN-4 are appreciably lower than most of the reported NiFe hydroxide-based analogues and other TM-based OER electrocatalysts (Fig. 4d[8,10,14,15,19,22,38,40,45-52] and Table. S8, Supporting Information), especially at large current densities (500 or 1000 mA cm⁻²), such as NiFe(OH)_x/FeS/IF ($\eta_{500} = 304$ mV, $\eta_{1000} = 332$ mV)[45], boronized SUS304 ($\eta_{500} = 420$ mV)[10], Ni-Fe-OH@Ni₃S₂/NF ($\eta_{500} = 370$ mV, $\eta_{1000} = 469$ mV)[52], which indicate the NiFe-LDH@DFN-4 has great potential to achieve commercial application of OER with low electric energy consumption. Moreover, the NiFe-LDH@DFN-4 exhibits a smaller Tafel slope of 34.7 mv dec⁻¹ compared with that of the NiFe-LDH@BFN (36.4 mv dec⁻¹) and NiFe-LDH@NF (40.0 mv dec⁻¹), suggesting faster OER kinetics when DFN-4 served as conductive substrate (Fig. 4b).

Nevertheless, the intrinsic catalytic activity and long-term stability of electrode can be more fundamental for evaluating OER performance. Here, we investigate the intrinsic catalytic activity of OER by normalizing current densities with electrochemical active surface area (ECSA). The ECSA values were estimated using an electrochemical capacitance measurement method (Fig. S30). Compared with the NiFe-LDH catalyst supported on commercial NF, the intrinsic catalytic activity of NiFe-LDH catalyst supported on BFN is increased, implying the strong catalyst-support interaction between NiFe-LDH catalyst and substrate of FeNi alloy[7] (Fig. 4c). Notably, the NiFe-LDH@DFN-4 exhibits the higher intrinsic catalytic activity than the NiFe-LDH@BFN, which generates a current density of 10 mA cm⁻²_{ECSA} at an extremely low overpotential of 243 mV, suggesting the stronger catalyst-support interaction induced by exposed FeNi(220) facet. Moreover, we note that the NiFe-LDH@DFN-4 shows an outstanding intrinsic catalytic activity, which is comparable to that of previously reported state-of-the-art catalysts, especially Ni_{0.8}Fe_{0.2}-amorphous oxyhydroxide nanowire arrays (Ni_{0.8}Fe_{0.2}-AHNA, the reported lowest value of η_{10} ECSA = 255 mV)[18] (Fig. 4e and Table. S9).

Besides, the long-term durability is a key parameter to evaluate the potential of industrial large-scale applications. The OER electrode must be stable for a long period under large current density operation conditions. Here, the durability of the NiFe-LDH@DFN-4 was tested by chronopotentiometric measurement in 1 M KOH at six constant current densities (10, 100, 250, 500, 1000 and 10 mA cm⁻²) for a total of 48 h. As shown in Fig. S31, the real-time potential remains almost unchanged throughout 48 h test period. Furthermore, the long-term durability of the NiFe-LDH@DFN-4 was checked in 1 M KOH and room temperature at a constant current density of 1000 mA cm⁻². Surprisingly, the operating potential almost does not increase after 1350 h (Fig. 4f). However, there is still a certain gap between such mild conditions (1 M KOH and room temperature) and harsh industrial application criterions (30 wt%

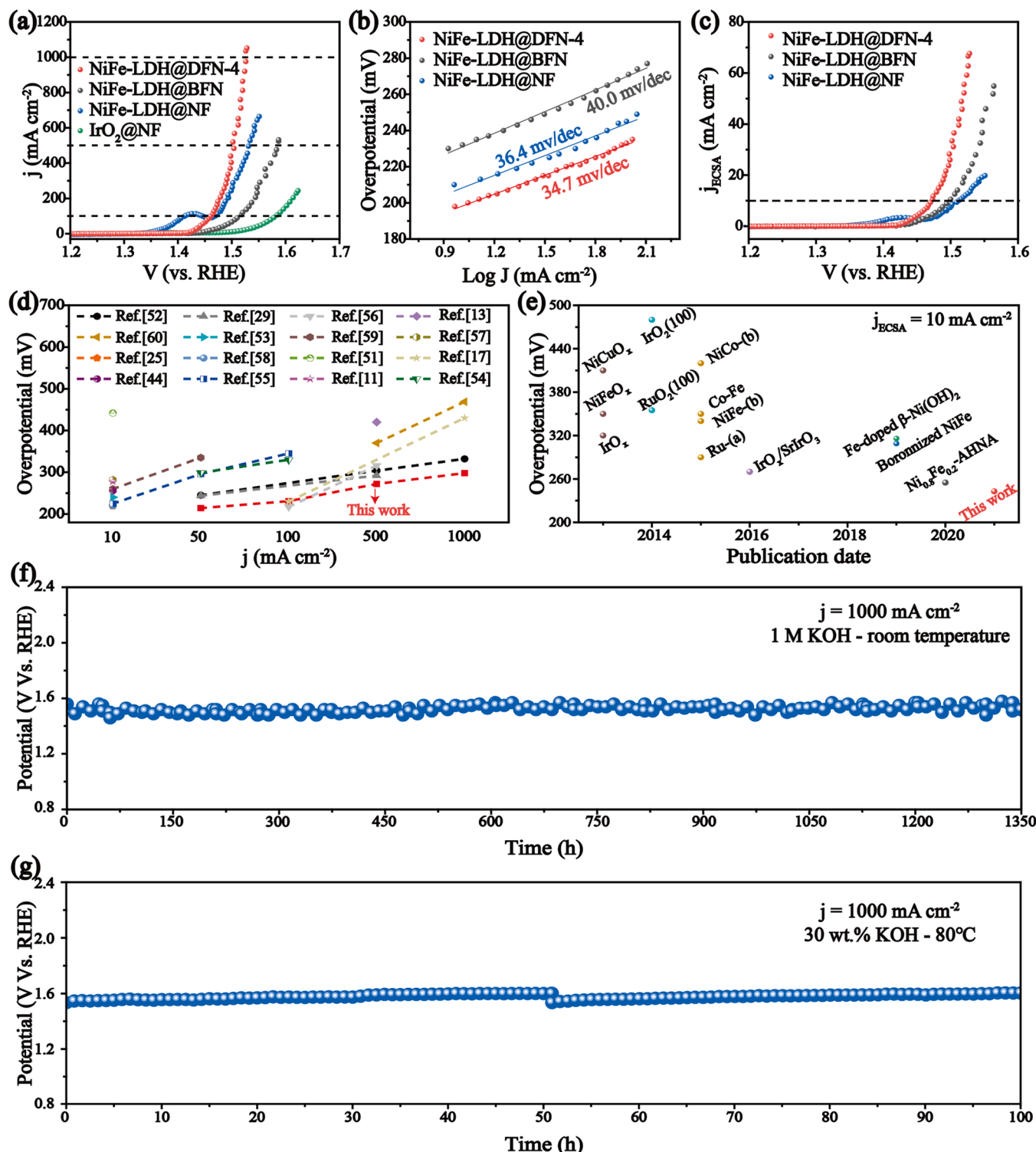


Fig. 4. Electrochemical characterizations. (a) OER polarization curves of as-prepared self-supported electrodes and IrO_2/NF in 1.0 M KOH at a scan rate of 5 mV s⁻¹, the overpotential (η) is calculated as follows: $\eta = V \text{ (vs.RHE)} - 1.23$. (b) Corresponding Tafel plots of as-prepared self-supported electrodes for OER. (c) OER polarization curves of as-prepared self-supported electrodes based on ECSA. (d) Comparison of the overpotentials required to reach the current densities of 10 mA cm⁻², 50 mA cm⁻², 100 mA cm⁻², 500 mA cm⁻², 1000 mA cm⁻², among our self-supported electrode and available reports. (e) Comparison of intrinsic catalytic activities (the overpotentials at ECSA normalized current density of 10 mA cm⁻²). (f) Long-term durability test in 1 M KOH at a constant current density of 1000 mA cm⁻² and room temperature for the NiFe-LDH@DFN-4. (g) Long-term durability test in 30 wt% KOH at a constant current density of 1000 mA cm⁻² and the industrial temperature of 80 °C for the NiFe-LDH@DFN-4. The NiFe-LDH@DFN-4 exhibits ultra-low overpotential and long-term durability under the harsh operating conditions of large current density.

KOH and 60–80 °C), which is rarely evaluated in previously reported OER electrodes. Therefore, we also performed a long-term durability test in 30 wt% KOH at a constant current density of 1000 mA cm⁻² and the industrial operating temperature of 80 °C for the NiFe-LDH@DFN-4. As shown in Fig. 4g, the increase of overpotential is negligible even after 100 h, indicating excellent durability under harsh operating conditions. These long-term stability tests indicate the NiFe-LDH catalyst supported on DFN-4 possesses excellent robustness under harsh operating conditions. Such superior stability is not available in previously reported NiFe-LDH catalyst supported on other substrates [5–7, 21, 41], confirming the DFN-4 substrate plays an important role in stabilizing the active sites of NiFe-LDH catalyst.

3.5. Mechanistic insight into the OER performance: strong catalyst-support interaction and reasonable three-phase interface

Above results show that the NiFe-LDH@DFN-4 exhibits outstanding intrinsic catalytic activity and long-term stability, demonstrating the DFN-4 is more suitable as the porous conductive substrate of self-

supporting OER electrode compared with commercial NF. We propose that this excellent performance originates from the following two aspects. One is the stronger catalyst-support interaction induced by the reasonable designed porous FeNi substrate with exposed high energy facets, and it will be discussed as following. First of all, we investigate the OER activity of nickel-based hydroxide (NH) supported on different conductive substrates by DFT calculations (see the *Supporting Information* for details, the calculated models were denoted as NH-FeNi(220), NH-FeNi(111) and NH-Ni(111), respectively). Fig. 5a shows the optimized OER pathways of NH-FeNi(220). Based on Gibbs free energy diagram (Fig. 5b), the rate-determining step of NH-FeNi(220) is the formation of *OH with ΔG of 1.91 eV and the theoretical overpotential (see the *Supporting Information* for details of the calculated formula) is 0.71 V. In comparison, the theoretical overpotential of NH-FeNi(111) and NH-Ni(111) are 0.82 V and 0.91 V, respectively. This suggests that the process of reaction intermediates adsorption is optimized on the surface of nickel-based hydroxide supported on FeNi(220) substrate, resulting in higher intrinsic catalytic activity, thus indicating the stronger catalyst-support interaction induced by (220) facets of FeNi

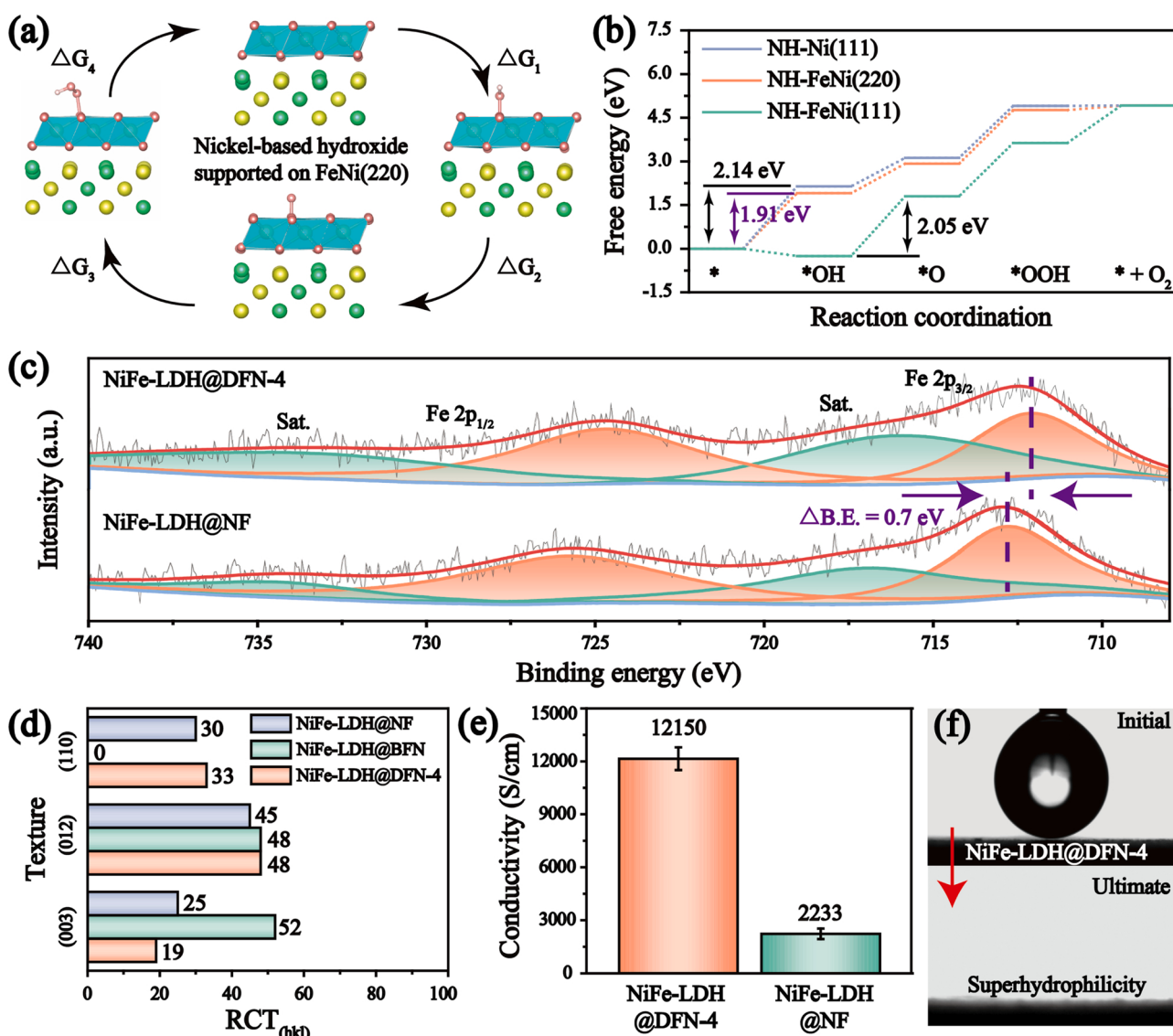


Fig. 5. The origin of high catalytic activity of NiFe-LDH@DFN-4. (a) Proposed OER pathways for nickel-based hydroxide (NH) supported on FeNi(220) substrate. (b) Gibbs free energy diagram for the OER on different models. (c) The high-resolution XPS spectra in the regions of Fe 2p after OER, the characteristic peaks of Fe³⁺ appear at around 712.0 and 712.7 eV for NiFe-LDH@DFN-4 and NiFe-LDH@NF, respectively. (d) Histograms for fitted relative texture coefficient (RTC) of NiFe-LDH according to the results of Fig. 3b. (e) The electronic conductivity. (f) The water contact angle of the NiFe-LDH@DFN-4.

alloy, compared with (111) facets of FeNi or Ni. However, such interactions exist thickness-dependent effect that the enhancement of catalytic activity becomes weak with the increase of the thickness of catalyst, which can't explain well much higher intrinsic catalytic activity. Therefore, there may be another mechanism jointly contributes to the significant improvement in the OER performance of the NiFe-LDH@DFN-4. The XPS results of the NiFe-LDH@DFN-4 and the NiFe-LDH@NF show that there is no significant change before and after OER (Fig. 3c, Fig. S21, Fig. S23, Fig. 5c and Fig. S32). However, it should be noted that the Fe 2 P XPS spectra reveal that the NiFe-LDH@DFN-4 exhibits a slight peak shift (0.7 eV) to lower binding energy compared with the NiFe-LDH@NF in spite of before or after OER, implying the lower valence states of Fe^{3+} on the surface of NiFe-LDH (Fig. S21b, Fig. S23b and Fig. 5c). The lower valence states of Fe^{3+} make it more difficult to oxidize Ni^{2+} in the NiFe-LDH matrix during the OER process, which can be confirmed by the redox couple anode shifts of CV curves (Fig. S33), leading to the suppression of the oxidation of $\text{Ni}(\text{OH})_2$ to NiOOH [53,54]. This character can be beneficial for increasing the oxidizing power of $\text{Ni}^{3+/4+}$ and thus facilitating OER kinetics[10, 53–55]. The lower valence states of Fe^{3+} in the NiFe-LDH@DFN-4 can be attributed to the *in situ* formation of Fe^{2+} via oxidation of Fe atoms in the DFN-4 matrix by Fe^{3+} from reaction solution during the process of hydrothermal treatment. Obviously, the NiFe-LDH@BFN (as presented in Fig. S22b and Fig. S34) will also display such phenomenon, while its intrinsic catalytic activity still is not comparable to that of the NiFe-LDH@DFN-4. We further calculate the relative texture coefficient of NiFe-LDH phase for the NiFe-LDH@DFN-4, NiFe-LDH@BFN and NiFe-LDH@NF electrodes (Fig. 5d). The RTC₍₀₀₃₎ of the NiFe-LDH@BFN and NiFe-LDH@NF are 52 and 25, respectively, which is much higher than that of the NiFe-LDH@DFN-4 (RTC₍₀₀₃₎ = 19), indicating the main preferred orientations of the NiFe-LDH@DFN-4 are (012) and (110) facets whose intrinsic catalytic activity is higher than (003) facets[5]. This is the reason why the NiFe-LDH@DFN-4 exhibits higher intrinsic catalytic activity compared with the NiFe-LDH@BFN. Furthermore, hydroxides are more favorable to nucleate and grow on the surface of FeNi(220) substrate at the process of hydrothermal treatment due to the superior wettability and lower adsorption energy of OH^- , resulting in a higher adsorption strength of NiFe-LDH on the FeNi(220) substrate that leads to the stabilization of active sites, thus contributing to the unique of long-term stability. Above results confirm the stronger catalyst-support interaction induced by the reasonable designed porous FeNi layer with exposed high energy facets on bulk materials, that our designed FeNi(220) substrate has strong synergistic effect on reaction intermediates adsorption on the surface of NiFe-LDH, valence state and main preferred orientations of NiFe-LDH, as well as the adsorption strength between NiFe-LDH and substrate.

The other aspect for excellent OER performance is the more reasonable three-phase interface of higher conductivity and better wettability because of using the reasonable designed DFN-4 as substrate, suggesting the DFN-4 is a promising substitute for commercial NF substrates. As shown in Fig. 5e, the NiFe-LDH@DFN-4 exhibits superior electronic conductivity of 12150 S cm^{-1} , which are 5.4 times more than that of the NiFe-LDH@NF. Besides, Nyquist plots and fitting results of equivalent circuit (Fig. S35 and Table. S10) also demonstrates that the NiFe-LDH@DFN-4 possesses the smallest charge transfer resistances (R_{ct}), indicating the fastest electron transfer kinetics of OER on the NiFe-LDH@DFN-4. We attribute the higher conductivity of the NiFe-LDH@DFN-4 to the electron transport highway provide by dense core of the DFN-4 and great adsorption strength of NiFe-LDH on the DFN-4. Furthermore, it can be seen that the droplet immediately disappears after touching the surface of the NiFe-LDH@DFN-4 (Fig. 5f), demonstrating much better superhydrophilic and superaerophobic after NiFe-LDH loading[27,35]. In sharp contrast, a droplet maintains a stable shape with a contact angle of $\sim 70^\circ$ after landing on the surface of NiFe-LDH@NF (Fig. S36). Thus, the NiFe-LDH@DFN-4 exhibits more reasonable three-phase interfaces, demonstrating this self-supporting

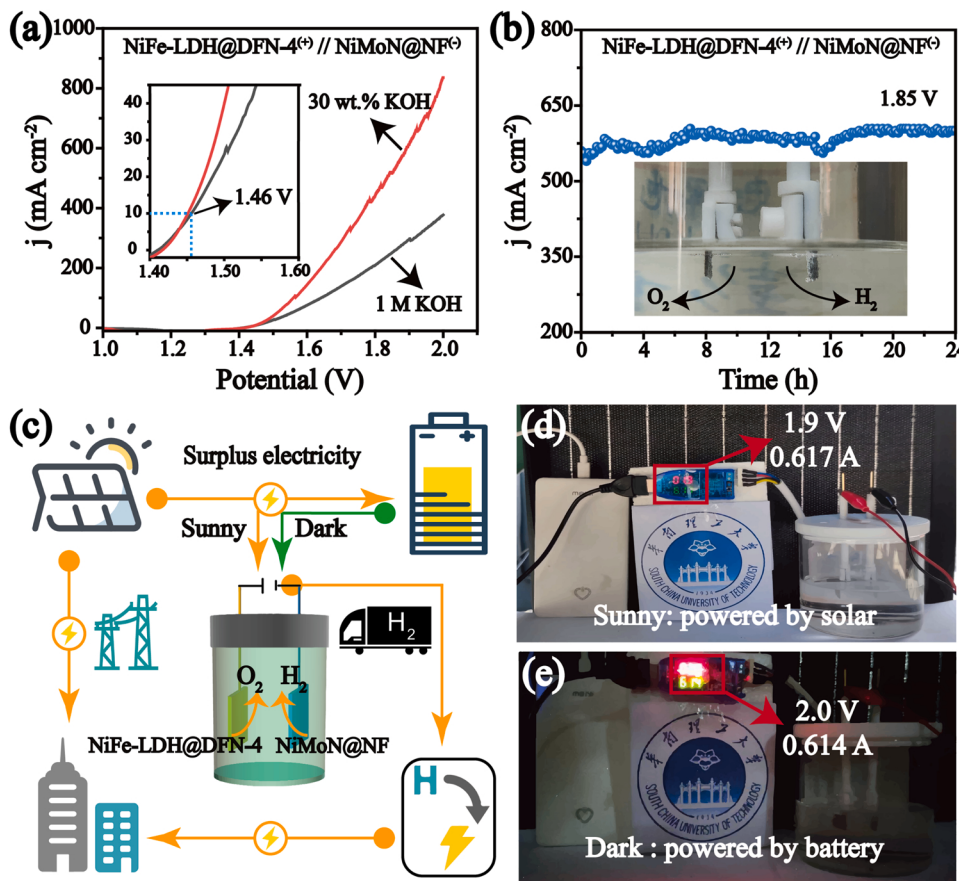
electrode is conductive to facilitating the reaction kinetics under harsh operating conditions, also leading to high intrinsic catalytic activity and excellent long-term stability.

3.6. Evaluation of practical application

To verify the potential of the NiFe-LDH@DFN-4 electrode for industrial applications, it is desirable to investigate overall water splitting without iR compensation. The commercial Pt/C@CC (Pt/C catalyst supported on carbon cloth) electrode was employed as HER electrode to paired with the NiFe-LDH@DFN-4, considering Pt-based catalysts have been regarded as the most proven and active HER catalysts. Herein, we performed a long-term durability test in 30 wt% KOH at a constant current density of 1000 mA cm^{-2} and the industrial operating temperature of 80°C for the NiFe-LDH@DFN-4⁽⁺⁾//Pt/C@CC⁽⁻⁾. As shown in Fig. S37, the cell voltage can maintain at approximately 1.95 V for 150 h at least, verifying the superior stability and industrial value of the NiFe-LDH@DFN-4. However, Pt-based catalysts are not attractive for large-scale applications, limited by its scarcity and high cost. Thus, it is necessary to pair the NiFe-LDH@DFN-4 with economic transition metal-based HER electrode for further application demonstration. Herein, a high-performance HER self-supporting electrode of NiMoN@NF was synthesized (see the Supporting Information for details) according to the literature[56]. As shown in Fig. 6a, the NiFe-LDH@DFN-4⁽⁺⁾//NiMoN@NF⁽⁻⁾ requires only a cell voltage of 1.46 V (overpotential of 230 mV) to achieve a current density of 10 mA cm^{-2} in 1 M KOH, which is impressive and outperforms most of the recent reported systems of overall water splitting (Table. S11). Furthermore, NiFe-LDH@DFN-4⁽⁺⁾//NiMoN@NF⁽⁻⁾ can generate extremely high current densities of 100, 250 and 500 mA cm^{-2} at low cell voltages of 1.56, 1.67 and 1.83 V in 30 wt% KOH (red line of Fig. 6a). As for durability, it is remarkable that NiFe-LDH@DFN-4⁽⁺⁾//NiMoN@NF⁽⁻⁾ can generate a current density of more than 550 mA cm^{-2} for over 24 h with an operating voltage of 1.85 V in 30 wt% KOH (Fig. 6b), which exhibits a promising potential forward to industrial applications. More importantly, it should be noted that water electrolysis plays an indispensable role in a sustainable energy system for breaking the spatio-temporal constraints of renewable energy and solving the problems of energy conversion storage and transportation (Fig. 6c). Thus, a simple device was constructed for simulating this process of energy conversion. The geometrical area of both OER and HER electrodes is 1 cm^2 . The electrolytic cell or battery can be powered by the surplus electricity of solar directly in sunny, and the electrolytic cell delivers a current of approximate 0.6 A at a cell voltage of $1.9\text{--}2.0 \text{ V}$ for 4 h (Fig. 6d and Fig. S38). Subsequently, the electrolytic cell is derived by a battery at night and also generates a current of about 0.6 A at a cell voltage of 2.0 V (Fig. 6e). This applicable testing demonstrates the promising potential application of the NiFe-LDH@DFN-4 OER electrode in industrial large-scale water electrolysis system. Additionally, the NiFe-LDH@DFN-4 electrode with a large size of $45 \times 80 \text{ mm}^2$ can be easily obtained by such a preferential dealloying strategy in our lab (Fig. S39 and Fig. S40), confirming it can be directly scaled up to support catalysts, thus contributing to large-scale industrial production.

4. Conclusions

In summary, we have developed a cost-effective and industrially compatible dealloying strategy to fabricate porous FeNi layer with high active (220) facets as anodic conductive substrate for water splitting. Computational and experimental results show that porous FeNi(220) substrate (DFN-4) exhibits superior OER performance and can be considered as a promising substrate for self-supporting OER electrode. The current densities of 10 and 250 mA cm^{-2} for the DFN-4 can be achieved at low overpotentials of 301 and 370 mV in base, respectively, implying the excellent OER catalytic activity. Benefiting from a series of



advantages of reasonable designed DFN-4 substrate with exposed active facets, the self-supporting OER electrode of NiFe-LDH@DFN-4 exhibits stronger catalyst-support interactions and more reasonable three-phase interfaces compared with the NiFe-LDH@NF, resulting in high intrinsic activity and unique long-term stability. As a result, the NiFe-LDH@DFN-4 outperforms better intrinsic catalytic activity than that of the state-of-the-art OER materials, which can output a current density of 10 mA cm⁻²_{EC5A} with low overpotential of 243 mV, better than the reported lowest value of 255 mV[18]. Notably, the NiFe-LDH@DFN-4 can generate large current densities of 500 mA cm⁻² and 1000 mA cm⁻² at extremely low overpotentials of 272 mV and 298 mV respectively, and retains such catalytic activity for 1350 h at room temperature and over 100 h even at 80 °C. Thus, the intrinsic catalytic activity and long-term durability of the NiFe-LDH@DFN-4 can be improved significantly compared with using the commercial NF as substrate. Furthermore, we have constructed a NiFe-LDH@DFN-4⁽⁺⁾//NiMoN@NF⁽⁻⁾ alkaline water electrolyzer, which exhibits super-low voltage of 1.46 V for a current density of 10 mA cm⁻² in 1 M KOH and generates a current density of more than 550 mA cm⁻² for over 24 h at an operating voltage of 1.85 V in 30 wt% KOH. Our work provides a novel strategy to design superior generations of electrocatalytic supports and generates high-performance and outstanding-stability OER self-supporting electrodes to meet large-scale industrial water splitting applications.

CRedit authorship contribution statement

Weiliang Peng: Methodology, Investigation, Software, Writing – original draft, Visualization. **Yuyin Li:** Data curation, Formal analysis, Visualization. **Bin Yuan:** Writing – review & editing, Resources, Supervision, Validation. **Renzong Hu:** Supervision, Validation. **Zhengtang Luo:** Writing – review & editing, Resources, Validation. **Min Zhu:** Writing – review & editing, Resources, Validation.

Fig. 6. Water splitting and practical application. (a) Polarization curve of overall water splitting electrolyzer composed of NiMoN@NF as cathode and NiFe-LDH@DFN-4 as anode (without iR compensation). (b) Long-term durability of overall water splitting at a voltage of 1.85 V in 30 wt% KOH. The inset is an optical photograph of the water splitting electrolyzer. (c) Schematic diagram for a sustainable energy system based on water electrolysis to produce hydrogen powered by the surplus electricity of renewable energy. The optical photograph of the experimental device for the simulation of electric energy powered by solar in sunny (d) and battery in dark (e).

Declaration of Competing Interest

The authors declare that they have no known competing financial interests or personal relationships that could have appeared to influence the work reported in this paper.

Data Availability

Data will be made available on request.

Acknowledgements

This work was supported by the National Natural Science Foundation of China (No. 51621001 and No. 52231009). Z.L. acknowledge supports by the RGC (16304421), the Innovation and Technology Commission (ITC-CNERC14SC01), Guangdong Science and Technology Department (Project#:2020A0505090003), Research Fund of Guangdong-Hong Kong-Macao Joint Laboratory for Intelligent Micro-Nano Optoelectronic Technology (No. 2020B1212030010), Guangdong Science and Technology Department (Project#:2020A0505090003) and Shenzhen Special Fund for Central Guiding the Local Science and Technology Development (2021Szvup136).

Appendix A. Supporting information

Supplementary data associated with this article can be found in the online version at doi:10.1016/j.apcatb.2022.122171.

References

[1] M.F. Lagadec, A. Grimaud, Water electrolyzers with closed and open electrochemical systems, *Nat. Mater.* 19 (2020) 1140–1150.

[2] T. Zhang, Y. Liu, J. Yu, Q. Ye, L. Yang, Y. Li, H.J. Fan, Biaxially strained MoS₂ nanoshells with controllable layers boost alkaline hydrogen evolution, *Adv. Mater.* 34 (2022), e2202195.

[3] Y. Zhou, W. Hao, X. Zhao, J. Zhou, H. Yu, B. Lin, Z. Liu, S.J. Pennycook, S. Li, H. J. Fan, Electronegativity-induced charge balancing to boost stability and activity of amorphous electrocatalysts, *Adv. Mater.* 34 (2022), e2100537.

[4] Z.Y. Yu, Y. Duan, X.Y. Feng, X. Yu, M.R. Gao, S.H. Yu, Clean and affordable hydrogen fuel from alkaline water splitting: past, recent progress, and future prospects, *Adv. Mater.* 33 (2021), e2007100.

[5] J.-W. Zhao, Z.-X. Shi, C.-F. Li, L.-F. Gu, G.-R. Li, Boosting the electrocatalytic performance of NiFe layered double hydroxides for the oxygen evolution reaction by exposing the highly active edge plane (012), *Chem. Sci.* 12 (2021) 650–659.

[6] H. Gu, G. Shi, H.-C. Chen, S. Xie, Y. Li, H. Tong, C. Yang, C. Zhu, J.T. Mefford, H. Xia, W.C. Chueh, H.M. Chen, L. Zhang, Strong catalyst-support interactions in electrochemical oxygen evolution on Ni–Fe layered double hydroxide, *ACS Energy Lett.* 5 (2020) 3185–3194.

[7] Q. Xiang, F. Li, W. Chen, Y. Ma, Y. Wu, X. Gu, Y. Qin, P. Tao, C. Song, W. Shang, H. Zhu, T. Deng, J. Wu, In situ vertical growth of Fe–Ni layered double-hydroxide arrays on Fe–Ni alloy foil: interfacial layer enhanced electrocatalyst with small overpotential for oxygen evolution reaction, *ACS Energy Lett.* 3 (2018) 2357–2365.

[8] M.S. Balogun, W. Qiu, Y. Huang, H. Yang, R. Xu, W. Zhao, G.R. Li, H. Ji, Y. Tong, Cost-effective alkaline water electrolysis based on nitrogen- and phosphorus-doped self-supportive electrocatalysts, *Adv. Mater.* 29 (2017), 1702095.

[9] H. Liu, J. Lei, S. Yang, F. Qin, L. Cui, Y. Kong, X. Zheng, T. Duan, W. Zhu, R. He, Boosting the oxygen evolution activity over cobalt nitride nanosheets through optimizing the electronic configuration, *Appl. Catal. B: Environ.* 286 (2021), 119894.

[10] F. Guo, Y. Wu, H. Chen, Y. Liu, L. Yang, X. Ai, X. Zou, High-performance oxygen evolution electrocatalysis by boronized metal sheets with self-functionalized surfaces, *Energy Environ. Sci.* 12 (2019) 684–692.

[11] N. Wang, A. Xu, P. Ou, S.F. Hung, A. Ozden, Y.R. Lu, J. Abed, Z. Wang, Y. Yan, M. J. Sun, Y. Xia, M. Han, J. Han, K. Yao, F.Y. Wu, P.H. Chen, A. Vomiero, A. Seifitokaldani, X. Sun, D. Sinton, Y. Liu, E.H. Sargent, H. Liang, Boride-derived oxygen-evolution catalysts, *Nat. Commun.* 12 (2021) 6089.

[12] L. Jiang, N. Yang, C. Yang, X. Zhu, Y. Jiang, X. Shen, C. Li, Q. Sun, Surface wettability engineering: Co₃-Ni₃S₂ nanoarray electrode for improving overall water splitting, *Appl. Catal. B: Environ.* 269 (2020), 118780.

[13] L.L. Feng, G. Yu, Y. Wu, G.D. Li, H. Li, Y. Sun, T. Asefa, W. Chen, X. Zou, High-index faceted Ni₃S₂ nanosheet arrays as highly active and ultrastable electrocatalysts for water splitting, *J. Am. Chem. Soc.* 137 (2015) 14023–14026.

[14] F.S. Zhang, J.W. Wang, J. Luo, R.R. Liu, Z.M. Zhang, C.T. He, T.B. Lu, Extraction of nickel from NiFe-LDH into Ni₂P@NiFe hydroxide as a bifunctional electrocatalyst for efficient overall water splitting, *Chem. Sci.* 9 (2018) 1375–1384.

[15] H. Zhang, X. Li, A. Hähnel, V. Naumann, C. Lin, S. Azimi, S.L. Schweizer, A. W. Maijenburg, R.B. Wehrspohn, Bifunctional heterostructure assembly of NiFe LDH nanosheets on NiCoP nanowires for highly efficient and stable overall water splitting, *Adv. Funct. Mater.* 28 (2018), 1706847.

[16] H. Sun, Z. Yan, F. Liu, W. Xu, F. Cheng, J. Chen, Self-supported transition-metal-based electrocatalysts for hydrogen and oxygen evolution, *Adv. Mater.* 32 (2020), e1806326.

[17] Z.W. Seh, J. Kibsgaard, C.F. Dickens, I. Chorkendorff, J.K. Norskov, T.F. Jaramillo, Combining theory and experiment in electrocatalysis: Insights into materials design, *Science* 355 (2017) eaad4998.

[18] C. Liang, P. Zou, A. Nairan, Y. Zhang, J. Liu, K. Liu, S. Hu, F. Kang, H.J. Fan, C. Yang, Exceptional performance of hierarchical Ni–Fe oxyhydroxide@NiFe alloy nanowire array electrocatalysts for large current density water splitting, *Energy Environ. Sci.* 13 (2020) 86–95.

[19] T. Kou, S. Wang, J.L. Hauser, M. Chen, S.R.J. Oliver, Y. Ye, J. Guo, Y. Li, Ni foam-supported Fe-doped β -Ni(OH)₂ nanosheets show ultralow overpotential for oxygen evolution reaction, *ACS Energy Lett.* 4 (2019) 622–628.

[20] G. Zhang, J. Yuan, Y. Liu, W. Lu, N. Fu, W. Li, H. Huang, Boosting the oxygen evolution reaction in non-precious catalysts by structural and electronic engineering, *J. Mater. Chem. A* 6 (2018) 10253–10263.

[21] D. Zhou, Z. Cai, Y. Jia, X. Xiong, Q. Xie, S. Wang, Y. Zhang, W. Liu, H. Duan, X. Sun, Activating basal plane in NiFe layered double hydroxide by Mn²⁺ doping for efficient and durable oxygen evolution reaction, *Nanoscale Horiz.* 3 (2018) 532–537.

[22] W. Zhu, T. Zhang, Y. Zhang, Z. Yue, Y. Li, R. Wang, Y. Ji, X. Sun, J. Wang, A practical-oriented NiFe-based water-oxidation catalyst enabled by ambient redox and hydrolysis co-precipitation strategy, *Appl. Catal. B: Environ.* 244 (2019) 844–852.

[23] S. Chang, X. Huang, C.Y. Aaron Ong, L. Zhao, L. Li, X. Wang, J. Ding, High loading accessible active sites via designable 3D-printed metal architecture towards promoting electrocatalytic performance, *J. Mater. Chem. A* 7 (2019) 18338–18347.

[24] F.-Y. Chen, Z.-Y. Wu, Z. Adler, H. Wang, Stability challenges of electrocatalytic oxygen evolution reaction: From mechanistic understanding to reactor design, *Joule* 5 (2021) 1–28.

[25] F. Zeng, C. Mebrahtu, L. Liao, A. Katharina Beine, R. Palkovits, Stability and deactivation of OER electrocatalysts: A review, *J. Energy Chem.* 69 (2022) 301–329.

[26] Y. Wang, Y. Zou, L. Tao, Y. Wang, G. Huang, S. Du, S. Wang, Rational design of three-phase interfaces for electrocatalysis, *Nano Res.* 12 (2019) 2055–2066.

[27] G.B. Darband, M. Aliofkhazraei, S. Shamugam, Recent advances in methods and technologies for enhancing bubble detachment during electrochemical water splitting, *Renew. Sustain. Energy Rev.* 114 (2019).

[28] X. Lu, C. Zhao, Electrodeposition of hierarchically structured three-dimensional nickel–iron electrodes for efficient oxygen evolution at high current densities, *Nat. Commun.* 6 (2015) 6616.

[29] Y. Liu, X. Liang, L. Gu, Y. Zhang, G.D. Li, X. Zou, J.S. Chen, Corrosion engineering towards efficient oxygen evolution electrodes with stable catalytic activity for over 6000 h, *Nat. Commun.* 9 (2018) 2609.

[30] L. Lei, D. Huang, C. Zhou, S. Chen, X. Yan, Z. Li, W. Wang, Demystifying the active roles of NiFe-based oxides/(oxy)hydroxides for electrochemical water splitting under alkaline conditions, *Coord. Chem. Rev.* 408 (2020), 213177.

[31] Y. Yang, M. Luo, W. Zhang, Y. Sun, X. Chen, S. Guo, Metal surface and interface energy electrocatalysis: fundamentals, performance engineering, and opportunities, *Chem* 4 (2018) 2054–2083.

[32] C. Guo, Y. Zheng, J. Ran, F. Xie, M. Jaroniec, S.Z. Qiao, Engineering high-energy interfacial structures for high-performance oxygen-involving electrocatalysis, *Angew. Chem. Int. Ed.* 56 (2017) 8539–8543.

[33] J. Perdew, K. Burke, M. Ernzerhof, Generalized gradient approximation made simple, *Phys. Rev. Lett.* 77 (1996) 3865–3868.

[34] G. Kresse, J. Furthmüller, Efficient iterative schemes for *ab initio* total-energy calculations using a plane-wave basis set, *Phys. Rev. B* 54 (1996) 11169–11186.

[35] J. Yong, F. Chen, Y. Fang, J. Huo, Y. Yang, J. Zhang, H. Bian, X. Hou, Bioinspired design of underwater superaerophobic and superaerophilic surfaces by femtosecond laser ablation for anti- or capturing bubbles, *ACS Appl. Mater. Interfaces* 9 (2017) 39863–39871.

[36] Z. Wang, G. Yang, Z. Zhang, M. Jin, Y. Yin, Selectivity on etching: creation of high-energy facets on copper nanocrystals for CO₂ electrochemical reduction, *ACS Nano* (2016) 4559–4564.

[37] B. Mohanty, P. Bhanja, B.K. Jena, An overview on advances in design and development of materials for electrochemical generation of hydrogen and oxygen, *Mater. Today Energy* 23 (2022), 100902.

[38] D. Zhang, X. Kong, M. Jiang, D. Lei, X. Lei, NiOOH-decorated α -FeOOH nanosheet array on stainless steel for applications in oxygen evolution reactions and supercapacitors, *ACS Sustain. Chem. Eng.* 7 (2019) 4420–4428.

[39] M. Zhou, S. Guo, J. Li, X. Luo, Z. Liu, T. Zhang, X. Cao, M. Long, B. Lu, A. Pan, G. Fang, J. Zhou, S. Liang, Surface-preferred crystal plane for a stable and reversible zinc anode, *Adv. Mater.* 33 (2021), e2100187.

[40] X. Cui, B. Zhang, C. Zeng, H. Wen, S. Guo, Monolithic nanoporous Ni Fe alloy by dealloying laser processed Ni Fe Al as electrocatalyst toward oxygen evolution reaction, *Int. J. Hydrog. Energy* 43 (2018) 15234–15244.

[41] P. Li, X. Duan, Y. Kuang, Y. Li, G. Zhang, W. Liu, X. Sun, Tuning electronic structure of nife layered double hydroxides with vanadium doping toward high efficient electrocatalytic water oxidation, *Adv. Energy Mater.* 8 (2018), 1703341.

[42] B.R. Lu, D. Wang, C.L. Zhao, K. Zhu, J. Yan, G.L. Wang, D.X. Cao, K. Ye, The novel dual-category active sites of NiCoP/CoP as high-performance electrocatalyst for urea electrolysis and synergistic hydrogen production, *Mater. Chem. Front.* 6 (2022) 1681–1689.

[43] L. Sha, T. Liu, K. Ye, K. Zhu, J. Yan, J. Yin, G. Wang, D. Cao, A heterogeneous interface on NiS@Ni₃S₂/NiMoO₄ heterostructures for efficient urea electrolysis, *J. Mater. Chem. A* 8 (2020) 18055–18063.

[44] L. Sha, K. Ye, J. Yin, K. Zhu, K. Cheng, J. Yan, G. Wang, D. Cao, In situ grown 3D hierarchical MnCo₂O_{4.5}@Ni(OH)₂ nanosheet arrays on Ni foam for efficient electrocatalytic urea oxidation, *Chem. Eng. J.* 381 (2020), 122603.

[45] S. Niu, W.J. Jiang, T. Tang, L.P. Yuan, H. Luo, J.S. Hu, Autogenous growth of hierarchical NiFe(OH)_x/FeS nanosheet-on-microsheet arrays for synergistically enhanced high-output water oxidation, *Adv. Funct. Mater.* 29 (2019), 1902180.

[46] X. Teng, J. Wang, L. Ji, Y. Liu, C. Zhang, Z. Chen, Fabrication of three-dimensional multiscale porous alloy foams at a planar substrate for efficient water splitting, *ACS Sustain. Chem. Eng.* 7 (2019) 5412–5419.

[47] X. Xiong, C. You, Z. Liu, A.M. Asiri, X. Sun, Co-Doped CuO nanoarray: an efficient oxygen evolution reaction electrocatalyst with enhanced activity, *ACS Sustain. Chem. Eng.* 6 (2018) 2883–2887.

[48] M. Yao, B. Sun, N. Wang, W. Hu, S. Komarneni, Self-generated N-doped anodized stainless steel mesh for an efficient and stable overall water splitting electrocatalyst, *Appl. Surf. Sci.* 480 (2019) 655–664.

[49] B. You, Y. Sun, Hierarchically porous nickel sulfide multifunctional superstructures, *Adv. Energy Mater.* 6 (2016), 1502333.

[50] C.Z. Yuan, Z.T. Sun, Y.F. Jiang, Z.K. Yang, N. Jiang, Z.W. Zhao, U.Y. Qazi, W. H. Zhang, A.W. Xu, One-step in situ growth of iron-nickel sulfide nanosheets on FeNi alloy foils: high-performance and self-supported electrodes for water oxidation, *Small* 13 (2017), 1604161.

[51] W. Zhu, X. Yue, W. Zhang, S. Yu, Y. Zhang, J. Wang, J. Wang, Nickel sulfide microsphere film on Ni foam as an efficient bifunctional electrocatalyst for overall water splitting, *Chem. Commun.* 52 (2016) 1486–1489.

[52] X. Zou, Y. Liu, G.D. Li, Y. Wu, D.P. Liu, W. Li, H.W. Li, D. Wang, Y. Zhang, X. Zou, Ultrafast formation of amorphous bimetallic hydroxide films on 3D conductive sulfide nanoarrays for large-current-density oxygen evolution electrocatalysis, *Adv. Mater.* 29 (2017), 1700404.

[53] L. Trotochaud, S.L. Young, J.K. Ranney, S.W. Boettcher, Nickel–iron oxyhydroxide oxygen-evolution electrocatalysts: the role of intentional and incidental iron incorporation, *J. Am. Chem. Soc.* 136 (2014) 6744–6753.

[54] M.W. Louie, A.T. Bell, An investigation of thin-film Ni-Fe oxide catalysts for the electrochemical evolution of oxygen, *J. Am. Chem. Soc.* 135 (2013) 12329–12337.

[55] M. Gorlin, J. Ferreira de Araujo, H. Schmies, D. Bernsmeier, S. Dresp, M. Giech, Z. Jusys, P. Chernev, R. Krahnert, H. Dau, P. Strasser, Tracking catalyst redox states and reaction dynamics in Ni-Fe oxyhydroxide oxygen evolution reaction electrocatalysts: the role of catalyst support and electrolyte pH, *J. Am. Chem. Soc.* 139 (2017) 2070–2082.

[56] Y. Gong, L. Wang, H. Xiong, M. Shao, L. Xu, A. Xie, S. Zhuang, Y. Tang, X. Yang, Y. Chen, P. Wan, 3D self-supported Ni nanoparticle@N-doped carbon nanotubes anchored on NiMoN pillars for the hydrogen evolution reaction with high activity and anti-oxidation ability, *J. Mater. Chem. A* 7 (2019) 13671–13678.